# REPORT DOCUMENTATION PAGE

Public reporting burden for this collection of information is estimated to average 1 hour per response, including the time for r~~
the data needed, and completing and reviewing this collection of information. Send comments regarding this burden estin~~
reducing this burden to Washington Headquarters Services, Directorate for Information Operations and Reports, 1215 Jeff~~
Management and Budget, Paperwork Reduction Project (0704-0188), Washington, DC 20503

AFRL-SR-BL-TR-91-

0643

maintaining
estions for
he Office of

| 1. AGENCY USE ONLY (Leave blank) | 2. REPORT DATE | 3. REPORT TY |
|---|---|---|

| 4. TITLE AND SUBTITLE | 5. FUNDING NUMBERS |
|---|---|
| NONEQUILIBRIUM TURBULENCE STUDY USING HOLOGRAPHIC PARTICLE IMAGE VELOCIMETRY | AFOSR Grant No. F49620-98-1-0414 |

**6. AUTHOR(S)**

Byron Jones and Hui Meng

| 7. PERFORMING ORGANIZATION NAME(S) AND ADDRESS(ES) | 8. PERFORMING ORGANIZATION REPORT NUMBER |
|---|---|
| Department of Mechanical & Nuclear Engineering Kansas State University Manhattan, KS 66506 | |

| 9. SPONSORING / MONITORING AGENCY NAME(S) AND ADDRESS(ES) | 10. SPONSORING / MONITORING AGENCY REPORT NUMBER |
|---|---|
| Dr. Tom Beutner AFOSR/NA 801 N. Randolph St. RM 732 Arlington, VA 22203-1973 | |

**11. SUPPLEMENTARY NOTES**

**12a. DISTRIBUTION / AVAILABILITY STATEMENT**

Approved for public release;
distribution unlimited.

AIR FORCE OFFICE OF SCIENTIFIC RESEARCH (AFOSR)
NOTICE OF TRANSMITTAL DTIC. THIS TECHNICAL REPORT
HAS BEEN REVIEWED AND IS APPROVED FOR PUBLIC RELEASE
LAW AFR 190-12. DISTRIBUTION IS UNLIMITED.

**12b. DISTRIBUTION CODE**

**13. ABSTRACT (Maximum 200 Words)**

The primary objective of this project involved the development of a three-dimensional flow field measurement tool, viz. holographic particle image velocimetry (HPIV), for applications in turbulent and complex flows. Holography is a 3D imaging process that instantaneously captures the volumetric information of a test object. A fully automated off-axis HPIV system based on an injection-seeded dual-pulsed YAG laser and 3D data processing software has been implemented in the Laser Flow Diagnostics Lab (LFD). In this system, 90-degree particle scattering, dual reference beams, *in situ* reconstruction/data processing, and 3D velocity extraction based on a fast "Concise Cross Correlation" (CCC) algorithm are utilized.

To quantify and characterize the HPIV technique for diagnosing three-dimensional flow fields, the technique has been applied to both a simulated flow to provide accuracy analysis and in real flows to test its feasibility and functionality. The off-axis HPIV system was tested in an acoustically excited air jet and the wake of a surface-mounted tab in a water channel flow, giving instantaneous 3D velocity fields for both flows. The development of HPIV was an interactive process driven by the pursuit of answers to the critical questions in nonequilibrium turbulence. These critical questions imposed technical requirements, design guidelines, and guided the HPIV evolution.

## 20020107 090

| 14. SUBJECT TERMS | 15. NUMBER OF PAGES |
|---|---|
| | 16. PRICE CODE |

| 17. SECURITY CLASSIFICATION OF REPORT | 18. SECURITY CLASSIFICATION OF THIS PAGE | 19. SECURITY CLASSIFICATION OF ABSTRACT | 20. LIMITATION OF ABSTRACT |
|---|---|---|---|

# NONEQUILIBRIUM TURBULENCE STUDY USING HOLOGRAPHIC PARTICLE IMAGE VELOCIMETRY

Byron Jones and Hui Meng*
Department of Mechanical & Nuclear Engineering
Kansas State University
Manhattan, KS 66506

*Mailing Address: Dept. of Mechanical & Aerospace Eng., SUNY, Buffalo, NY 14260

## Abstract

The primary objective of this project involved the development of a three-dimensional flow field measurement tool, viz. holographic particle image velocimetry (HPIV), for applications in turbulent and complex flows. Holography is a 3D imaging process that instantaneously captures the volumetric information of a test object. A 3D distribution of particles is recorded by illuminating the particle field with an expanded laser beam and registering the scattered light (the object wave) on a holographic recording medium (film or plate) through the interference with a coherent reference wave (Figure 1a). The resultant hologram contains information about the "frozen" 3D particle field at the instant of exposure. The desired diagnostic information can be retrieved after the hologram is developed, usually by "reconstructing" the hologram, a 3D real image of the particle field, and then scanning the image volume through the acquisition of a series of densely spaced image planes along the optic axis (Figure 1b).

A fully automated off-axis HPIV system based on an injection-seeded dual-pulsed YAG laser and 3D data processing software has been implemented in the Laser Flow Diagnostics Lab (LFD). In this system, 90-degree particle scattering, dual reference beams, *in situ* reconstruction/data processing, and 3D velocity extraction based on a fast "Concise Cross Correlation" (CCC) algorithm are utilized.

To quantify and characterize the HPIV technique for diagnosing three-dimensional flow fields, the technique has been applied to both a simulated flow to provide accuracy analysis and in real flows to test its feasibility and functionality. The off-axis HPIV system was tested in an acoustically excited air jet and the wake of a surface-mounted tab in a water channel flow, giving instantaneous 3D velocity fields for both flows.

The development of HPIV was an interactive process driven by the pursuit of answers to the critical questions in nonequilibrium turbulence. These critical questions imposed technical requirements, design guidelines, and guided the HPIV evolution. The usefulness of any diagnostic technique can be roughly categorized into two major parts: firstly the accuracy and precision of the physical measurements and secondly the practical ease of use of the technique. An easy-to-use inaccurate or impossible-to-use accurate

instrument is of little scientific significance. Details on how the technical requirements and design guidelines where satisfied follow. The issues relating to HPIV measurement accuracy are quantified in the HPIV Accuracy section.

# 1 Rationale of the Off-axis HPIV Technique

Compared with in-line techniques, off-axis holography tolerates higher seeding densities and offers a much better image signal to noise ratio (SNR) because the directly transmitted wave and the virtual and real image waves are naturally separated during reconstruction. By utilizing wide-spread side scattering other than the narrow central-lob forward scattering of particles, the effective Numerical Aperture (N.A.) of imaging is drastically increased, thereby reducing the depth of focus and yielding higher measurement accuracy. Also the directional ambiguity problem inherent in double-exposure in-line HPIV can be solved by employing dual reference waves at different angles. These make off-axis HPIV a desirable configuration despite the optical complexities and the high requirements on the laser power and coherence. However, the particle scattering characteristics require a trade-off between the achievable effective N.A. and the laser energy utilization, since most of the laser energy scattered by the particles is carried by the narrow-angled forward scattering. Side scattering is much weaker than forward scattering and near-forward scattering, thus calling for much higher laser power/energy than what in-line versions require.

Various off-axis methods have been proposed and reported since the early years of HPIV development [1] [2] [3] [4] (Barnhart, *et al.* 1994; Meng 1994; Zhang *et al.* 1997), addressing the problem of laser energy utilization and effective N.A. Encouraged by the high scattering efficiency of the forward scattering, [3] Zhang *et al.* (1997) constructed a hybrid HPIV system, where forward scattering is combined with off-axis holography. In the configuration an optical high-pass spatial filter is utilized to avoid the directly transmitted wave in the object beam. In contrast, [1] Barnhart, *et al.* (1994) implemented a phase conjugate HPIV system, where two separate channels of near-forward scattering are combined to achieve an effective large N.A. of particle images. To compensate for the severe optical distortion and aberration imposed by the complex optics, a phase conjugate reconstruction system is required. These two approaches exemplify compromises between the laser energy utilization and the effective N.A.

Such compromises in off-axis HPIV often come with undesirable problems. In the system of [3] Zhang *et al.* (1997) the employment of the central-lob forward scattering and long recording distance results in low effective N.A. To make up for the large depth of focus, an extra hologram has to be placed in the orthogonal axis to provide the velocity component in the depth direction. Such a system involves not only doubling the amount of optics and data processing, strict coordination of the two orthogonal holograms, and synthesis of 3D vector map, but also requires the flow domain to be optically accessible from two orthogonal directions through four windows. On the other hand, the phase-conjugate off-axis HPIV system by [1] Barnhart *et al.* (1994) involves a different type of practical restriction. In spite of the low *f*-number lenses, the two-channel optical system used for collecting scattered light works effectively as a low-quality imaging system, introducing excessive optical aberrations that prohibit the reconstruction of particle

2

images. The only remedy is to employ the so-called phase-conjugate reconstruction, *i.e.* extract back tracing of optical waves from the hologram to the particle images. This requires placing *everything*, including the original flow medium and any walls or windows that appeared between the particles and the hologram during the recording, back into the reconstruction system. Often, this is not feasible, and when it is feasible (as in the case of an open jet in air with no walls), extremely strict alignment of hologram and optics is necessary. In addition, both of these off-axis HPIV systems described above resort to the use of a separate laser (a continuous-wave laser) for hologram reconstruction. Since misalignment and difference in wavefronts are inevitable, switching lasers introduces additional sources of image distortion and noise. Furthermore, when the recording and reconstruction lasers do not share the same wavelength, as with the approach of [3] Zhang *et al.* (1997), extra image aberration is generated from the wavelength difference.

Among the practical obstacles in HPIV application, noise is the most critical issue. While the use of off-axis holography eliminates the excessive speckle noise specifically associated with in-line holography [4] (Meng et al. 1993), other types of noise still exist, among which the superposition of reconstructed particle images in a volumetric region is the most prominent. This is because the light flux from those out-of-focus particle images in the real image field entering the pupil of the objective lens – although not imaged – can form a speckle noise background. Such noise increases with the particle seeding density and the depth of the image volume. The contribution of particle images far from the focal plane is a low-intensity, homogeneous white noise, and we denote it as trivial noise. In contrast, the contribution of particle images slightly out of focus is a localized high-intensity noise, and we denote it as critical noise. It is indicated that the increase of effective N.A. has different effects on these two kinds of noises. The trivial noise increases with increasing effective N.A. However, it can be filtered out easily, since its image characteristics including power spectrum is quite different from those of the effective image signal. On the other hand, the critical noise decreases with increasing effective N.A. because the image depth of focus becomes shorter, resulting in less image overlap. Since the critical noise is much harder to eliminate due to its similarity in characteristics to the effective image signal, an increase in effective N.A. improves the overall image quality.

Using these considerations, we propose a different solution than the past approaches to off-axis HPIV. A high effective N.A. is achieved by using 90-degree scattering, which provides homogeneous intensity distribution over a large solid angle [2] (Meng 1994), and by shortening the recording distance without adding any optics between the hologram and the particle field. The optical configuration of the 90-degree scattering HPIV resembles that of planar PIV to a large degree in that the flow facility is illuluminated from one direction and imaged captured from an orthogonal direction. This optical access is more suitable for most practical applications. It is appropriate to point out that since 90-degree scattering is rather weak, it is essential to minimize noise introduced by reflection of laser light on walls and optical components. The short recording distance also increases the efficiency of the laser energy utilization. To further increase particle image SNR we reduce reconstruction aberration by *in-situ* reconstruction. This involves the use

: same laser source and the same reference-beam optics for recording and
: :n.

: h image SNR achieved by the off-axis configuration alleviates the need for
: : the data processing stage and thus greatly improves the overall processing
: high SNR also brings a highly efficient, yet simple implementation of a
: roid finding algorithm. By utilizing only particle centroid locations instead of raw images, a compression ratio of several orders of magnitude has been achieved. This allows the use of a fast Concise Cross Correlation (CCC) algorithm, which works on particle centroids, thereby drastically improving processing speed over conventional cross-correlation.

## 2 HPIV Design Criteria

Validation of the HPIV measurement of velocity fields on a 3D grid is accomplished through examination of the continuity equation. In the example shown in Figure 2, it is found that the divergence has a mean value of $0.51s^{-1}$ and a standard deviation of $6.63s^{-1}$. To estimate the relative error, we evaluate the net flux $\Delta Q = \iiint_{CV} \nabla \cdot \mathbf{u} dV$ entering an arbitrary control volume $CV = \Delta x \Delta y \Delta z$, divided by the total flux $Q = U \cdot \Delta y \Delta z$ passing through the control volume: $\eta = \dfrac{\Delta Q}{Q}$. For an estimation of the worst case, we choose the 95% coverage divergence value and the smallest control volume size (the grid size), it is found from the experimental data that $\eta \sim 4.7\%$. Hence, continuity is satisfied reasonably well.

### 2.1 Speckle noise

For successful particle measurement using holography, it is necessary to control the amount of speckle noise to achieve an acceptable SNR. That means, for a given optical setup, the particle size, seeding density, and the total depth of the particle field along the path of light propagation have to be controlled within limits. For a given particle field, the highest SNR that traditional in-line holography can ever hope to attain (i.e. the upper bound of SNR) is approached under the asymptotic condition that the transmission of the direct current (dc) component of reference beam is zero [4] (Meng et al. 1993). Such an upper bound should be at least 15dB, under which condition the actual SNR with finite dc transmission will usually vary between 5 dB and 10 dB, which is considered sufficient in most cases. The condition that the upper bound of SNR > 15 dB can be expressed in terms of the "shadow factor", defined as the percentage of beam blockage by all the particles projected along the illumination path without overlap. It follows from Eq. (47) given by [4] Meng et al. (1993) that the shadow factor can be no more than 4%:

$$\frac{\pi}{4}d^2 n_s L < 4\% . \tag{1}$$

where $d$ is the particle diameter, $n_s$ the seeding density, and $L$ the total depth of the

4

particle field along the light propagation. This estimate works very well as experience has shown. As an example, if $d = 20$ μm, $L = 10$cm, the maximum particle seeding $n_s$ allowed for an in-line hologram is about 1.3 particles/mm³. The corresponding particle volume loading is $5 \times 10^{-6}$.

In practice, most multiphase flow applications involve particle densities higher than what traditional in-line holography could handle. For example, [5] Jones *et al.* (1978) concluded that in-line holography was essentially useless for the drop sizing in dense fuel sprays. Methods to improve the capacity of holography for handling larger particle loading involve elements of *off-axis* holography, where the reference wave is introduced at an angle to the object wave (Figure 1). An off-axis hologram reduces speckle noise drastically and allows the increase of the particle seeding density of up to two orders of magnitude over in-line holography. This is because in off-axis holography the real image, virtual image, and the transmitted beams during reconstruction are all separated such that they do not interfere with each other. Hence, in our current research we opt for off-axis holography for measuring particle fields.

## 2.2 Depth of focus

The light from forward scattering of a particle is concentrated mainly in a cone of a very small angle ($1.22\lambda/d$, $\lambda$ is the laser wavelength, $d$ is the particle diameter). This results in a large depth of focus of the particle images and hence poor accuracy along the depth direction. The depth of focus is traditionally defined as the maximum defocus distance from the exact image position that does not cause a significant change in the image. For a particle image formed by forward scattering, the depth of focus (bi-lateral) is

$$2\delta \approx \beta d^2 / \lambda, \tag{2}$$

where $d^2 / \lambda$ is the far-field number of the particle, and $\beta$ a coefficient greater than or equal to 1 [6] [7] (Meng and Hussain 1995a, 1995b). The value of $\beta$ is dependent on the specific optical arrangement, the threshold of the image acquisition camera (a higher threshold corresponds to a smaller β), as well as the data processing scheme. The last point is important since the data processing scheme determines the *effective* definition of the depth of focus. For example, while using the 2D auto-correlation to process their images, [3] Zhang *et al.* (1997) defined their depth of focus to be the range within which the intensity level of a particle image was distinctly higher than its background and the software would be able to pick it up as a particle. Using this criterion, they observed a mean depth of focus of 0.81 mm for $d = 15$ μm, $\lambda = 0.633$ μm in a hybrid optical arrangement where the zero-degree forward scattering was removed. This depth of focus value corresponds to $\beta \approx 2.3$ in Eq. (2). Although the removal of the zero-degree forward scattering in their system greatly reduced the particle image depth of focus compared to an in-line hologram, the resultant depth of focus value was still larger than what was reported by [6][7] Meng and Hussain (1995a, 1995b), where $\beta \approx 1$ and the depth of focus was defined by the distance with recognizable changes of intensity distribution. Despite the subjective nature of the definition of depth of focus, under the same experimental condition, forward scattering undoubtedly gives by far the largest

depth of focus. For example, by using the side scattering components (about $10^{\circ}$-$30^{\circ}$) in reconstruction, [6][7] Meng and Hussain (1995a, 1995b) reported a 10-fold reduction of depth of focus from the standard in-line scheme.

With off-axis holography, where the object beam is separate from the reference beam, it is much easier to employ the side scattering instead of forward scattering of particles for hologram recording, hence allowing drastic reduction of the depth of focus of particle images. Side scattering, especially around $90^{\circ}$, spreads its intensity across a wide angular range, and hence the effective aperture $\Omega$ is determined by the hologram and the viewing optics. The depth of focus can be evaluated as [6][7] (Meng and Hussain 1995a, 1995b):

$$2\delta \approx 2\beta d / \Omega. \tag{3}$$

This is almost always smaller than that determined from Eq. (2).

Based on the above considerations and with the particle position and velocity measurements as our main objectives, the $90^{\circ}$ scattering off-axis holography configuration was chosen for the current HPIV for particulate flows. This allows us to extract individual particle positions and enables the use of the CCC algorithm, which preserves particle velocities. The fully automated off-axis HPIV system has been described in detail by [8] Pu & Meng (2000) in the context of velocimetry only. In what follows we explain briefly the hologram recording and reconstruction phases, as illustrated in Figure 3.

## 3  System Description

Based on the off-axis holography principle, a fully automated experimental off-axis HPIV, which employs 90-degree scattering, dual reference beams, in-situ reconstruction, and novel 3D data processing algorithms was implemented. At the core of HPIV data processing, a fast Concise Cross Correlation algorithm for velocity extraction based on particle centroids was employed. The CCC process consists of correlation based on centroids and (optional) particle pairing. While correlation results are always statistical averaging of particle groups, by pairing individual particles in the correlation sets using correlation results as a reference, super resolution [9] (Keane, *et al.* 1995) is achieved. The paired vectors are actually individual particle velocities, and the positions of these particles are already extracted through centroid finding. Such information on *individual* particles offers more possibilities for the applications of our off-axis HPIV technique. In this section the HPIV system is described in detail.

### 3.1  Recording

Recording of particle images is the first step in HPIV measurement. Illustrated in Figure 4 is the optical configuration for off-axis HPIV recording. An injection-seeded dual Nd:YAG laser (Spectra-Physics PIV-400) is employed, which gives a pair of temporally and spatially separated laser pulses, each of 8ns duration, at a repetition rate of

10Hz. Thus, the system is capable of double exposure to provide particle velocity measurement.

As in regular PIV applications, the double pulse separation $\Delta t$ is adjusted according to the estimated flow speed. The two laser units contained in the dual YAG laser system are fired by a multi-channel digital delay generator. The addition of injection seeding to the standard PIV-400 laser guarantees sufficient coherence length (over a meter). The increased coherence length enables high-quality off-axis holographic recording of a large volume while allowing unmatched optical path lengths between object and reference beams. To ensure the stability of injection seeding operation, the pulsed laser system has to fire constantly during the recording process, and hence a pair of high-energy shutters operated through a synchronizer are needed to generate a single pair of laser pulses. The synchronizer assures each shutter to pass one and only one laser pulse each time.

Each laser head emits a beam, which, after passing through a shutter and a pair of high-energy mirrors (HEM), is split into two parts by a partial reflection mirror which works as a beam splitter (BS). The majority of the energy (80%) from each beam is reflected and used for illumination. The two illuminating beams, very close to each other, are combined at a common receiving HEM. The slight angular misalignment between the two beams becomes negligible after they pass through the illuminating beam expander. The transmitting part of each laser beam through the BS is further manipulated by a variable beam splitter (VBS), which consists of a pair of half-wave plates (WP) and a polarizing beam splitter (PBS). With the two VBS, it is possible to adjust the intensity of the reference beams and thus the reference-to-object intensity ratio. Evidently, the beam handling unit (enclosed by dashed line on the bottom-right corner of Figure 4) produces three output beams: two separate reference beams (Reference 1 and 2) and one combined illuminating beam. It actually works as a multiplexer during double exposure: the illuminating beam is double pulsed, while the two reference beams are alternately single pulsed. This dual-reference-beam design provides angular separation of the reference beams for the double-exposure hologram, so that the two holographic images can be reconstructed alternately in time.

Three beam expanders are used to collimate the three beams and expand them into proper sizes: 3~5" diameter for the illuminating beam and 3" diameter for the reference beams. Since there is no special requirement on the quality of the illuminating beam, the beam expander needed is rather simple, consisting of a concave lens (for expanding) and a convex lens (for collimating). The two reference beams, however, should be high-quality plane waves for easy reproduction during the reconstruction (even with our *in situ* reconstruction, plane waves are preferred for producing conjugation beams). Hence, two factory-assembled beam expanders are used here. The reference beams are then bent over by a pair of flat mirrors to the holographic plate, which has its emulsion side facing the particle field (the flow region). The 90-degree scattered light from the particle field interferes with the reference beams, and the resultant interference pattern is recorded by the holographic plate. In this way a 90-degree-scattering dual-reference off-axis HPIV recording scheme is created.

Reference-to-object intensity ratio (R-O ratio) is one of the most crucial parameters in making successful holograms. In particle holography, where the object wave is a

complex superposition of numerous weak near-spherical waves scattered by individual particles, R-O ratio plays an even more critical role. Both the R-O ratio based on individual scattering and the R-O ratio based on overall scattering intensity are important. First, it is the scattering from the individual particles that is responsible for forming the useful fringes on the hologram, hence the need for appropriate R-O ratio based on individual particles. Second, the holographic film has a finite dynamic range for exposure energy. Since the film responds to the summation of the light energy at every point, the R-O ratio based on overall scattering intensity must be controlled. From a practical point of view, it is easier to work with the overall scattering intensity for the whole particle field since it is much more measurable and controllable than the scattering intensity of individual particles. Besides, its influence on film dynamic range is rather critical. The individual scattering R-O ratio has been found to have a rather high tolerance [2] (Meng 1994), allowing some variations of the particle ensemble size under a given overall R-O ratio. For the range of the image volume (1~3") and the seeding density we are currently interested in, an overall R-O ratio of 5:1 is found optimal in most cases. Understandably, its tolerance is closely related to the particle seeding density and image volume in the actual flow measurement.

## 3.2 Reconstruction

After the hologram is recorded and chemically processed, the 3D particle information contained within must be reconstructed -- normally optically. To minimize aberrations so as to ensure high SNR, we reconstruct the holograms *in situ*, where exactly the same laser and the same reference beams used for recording are employed. This unconventional approach has proven very effective and convenient. As shown in Figure 5, the hologram reconstruction system shares the same optics as the recording system, except that the object illustrating beam is blocked since it is no longer needed during reconstruction. The developed hologram containing interference fringes is now placed back at the original position, albeit with the film emulsion facing opposite to that of recording, such that each reference beam incident on the hologram becomes the complex conjugate of that used in recording. In this way, an unscrambled real image of the 3D particle field is reconstructed on the emulsion side, *i.e.*, on the opposite side to the flow field.

The laser shutters are kept open at all times to pass every laser pulse for continuous hologram reconstruction and image acquisition. The two laser units are fired alternately, each at 10Hz, to produce the two reference beams corresponding to those used for double-exposure recording. This way, the hologram alternately reconstructs the particle field recorded before and after the double exposure $\Delta t$.

Now that a frozen 3D particle field from each exposure is reconstructed continuously, it can be interrogated with a planar imaging device to be converted into digital form. A high-resolution digital CCD camera (KODAK ES1.0, 1k×1k, 30fps) mounted on a 3D traversing system (Daedal-Parker) is employed to capture the reconstructed holographic image. The camera sees only a small area of a thin slice at a time. The 3D image is interrogated slice by slice, and area by area. The entire particle field is thus decomposed into many 3D Interrogation Cells (IC), similar to the 2D Interrogation Spots (IS) in planar PIV. The pitch in depth direction, *i.e.* the distance

8

between adjacent slices, must be small enough to resolve particle images along the depth direction. The IC size affects the processing speed and measurement accuracy, as well as the SNR of the acquired image. The choice of a larger IC size enables faster processing but also leads to a longer effective depth of focus of the particle image as seen by the CCD camera. This is because in order to increase the camera viewing area (zoom out), the effective N.A. of the objective lens on the CCD camera must be reduced. The increased depth of focus not only degrades measurement accuracy, but also causes interference of out-of-focus particle images, producing random spots or speckle noise. Therefore a compromise between the processing speed and the measurement accuracy is unavoidable.

In the current system data acquisition and processing are fully automated and controlled by a PC. A PCI digital image framegrabber is hosted in the computer to perform image capturing, and a motion controller is also installed to position the camera through the 3-axis traverse system. Image acquisition and camera movement are synchronized with the laser pulses to ensure data integrity. Data processing is completed on the fly, given that the processing is fast enough to follow the image acquisition and camera positioning. A speed of approximately one pair of image planes per second is achieved by the system.

## 4 Data Processing

Figure 6 is a schematic diagram of the data processing algorithm used in the off-axis HPIV system. Digital images captured by the CCD camera are transferred into the system memory in the host computer via the framegrabber. The scanned 3D particle images contain a tremendous amount of data. Since the particle size and shape are not among the objectives of HPIV measurement, we compress the data into a list of particle centroid locations. To further obtain particle velocities, we correlate two particle centroid files corresponding to the two exposures made on the hologram using CCC algorithm, which consists of correlation and particle pairing.

### 4.1 Centroid Finding

It is well recognized that the centroid finding process is the bottleneck of the processing speed since it is the data compression stage. Hence the centroid finding is critical to processing efficiency. Fortunately, because of the high image quality of the off-axis holography based on 90-degree particle scattering, no de-noising operation is needed in the centroid finding process.

In the digitized image frames an image of a particle is a 3D cluster of pixels with high intensity. Two methods are used to obtain particle centroids. The first method assumes that the intensity peak of a particle image is typically located at its geometric center. To calculate the 3D centroid location of a particle we adopted the intensity-weighted-mean coordinates [10] (Gonalez and Woods, 1993):

$$\sum_{m=1}^{n} x_m I_m \bigg/ \sum_{m=1}^{n} I_m$$

$$\sum_{m=1}^{n} y_m I_m \bigg/ \sum_{m=1}^{n} I_m \quad (4)$$

$$= \sum_{m=1}^{n} z_m I_m \bigg/ \sum_{m=1}^{n} I_m$$

where $x_c$, $y_c$, and $z_c$ are the centroid coordinates, $x_m$, $y_m$, and $z_m$ are the *mth* pixel in a 3D particle image, and $I_m$ is its intensity, and $n$ is the number of pixels in one particle image.

### 4.1.1  Particle Reconstruction by Pixel Clustering Method

To extract centroids by applying Eq. (4), pixels making up the same particle images must be clustered, and noise pixels must be filtered out. This process consists of intensity thresholding and centroid computation, followed by further noise filtering based on 3D intensity summation of particle images. At first, an appropriate intensity threshold is set to separate particles from the background. Then a list of particle centroids is created and updated throughout the search in the image volume. Each element in the centroid list corresponds to a particle image, consisting of the 3D coordinates of the centroid and total intensity of the pixel cluster. During the process, the first pixel found above the intensity threshold becomes the first element in the list, and subsequently all other pixels in the image field are searched to build the centroid list. At any step, a pixel with intensity above the threshold is compared with other elements in the centroid list. If it is found to be in the proximity (within 8 pixels in x- and y- direction and 4 planes in z-direction) of an existing centroid in the list, it is considered a part of the same particle image. The data of this centroid is updated according to Eq. (4) to accommodate the new member in the cluster. If it is not in the proximity of any centroids, it is added to the list as a new particle centroid.

Even after the thresholding, the extracted centroid file may still contain noise, or false particles. This noise can be further reduced through CCC. We will show that CCC has certain tolerance to false particles.

As we perform image scanning and centroid finding, the energy of the laser beam to reconstruct the hologram often fluctuates from pulse to pulse. This fluctuation is translated into intensity variation between interrogation cells and between different planes within the same 3D particle image, affecting the criteria of intensity threshold and thus affecting accuracy of particle centroids. To overcome this problem, we employ an adaptive threshold calculated based on the histogram of intensity in a plane that the CCD camera captures. Illustrated in Figure 7 is a typical intensity histogram obtained from a plane in the reconstructed image. The particle images consist of pixels with high intensities, which appear to be a peak on the high intensity side of the histogram. Statistically they consist of an almost constant percentage of the whole image pixels. Since the laser pulse fluctuation has little effect on the profile of the histogram but only causes it to shift as a whole, we can set the intensity threshold at a certain percentage of the total pixels. Immediately after each image is acquired by the computer, its histogram

is computed. The threshold is then calculated by counting pixels from the highest intensity down to the lowest side until a fixed percentage of pixels is included.

The accuracy of centroid locations is asymmetric along the three directions. In x- and y-directions (camera sensor plane) pixels are usually a few microns apart. In z-direction, however, sample points are on discrete image planes, whose pitch distance (between two adjacent planes) is typically 50-200μm depending on the image depth of focus and desired data processing speed. Therefore the z-coordinate in the centroid finding requires a "sub-pixel" resolution for higher accuracy.

The uncertainties in finding particle centroids are the primary sources of error in the paired vector field. Therefore it is important to quantify such uncertainties. For this purpose we use simulated 3D particle images to examine the centroid extraction algorithm. In the simulations, numerically generated particles are randomly distributed in a given volume and projected onto a series of planes throughout the volume. The image planes are fed to the centroid finding algorithm. The extracted centroids are then compared with those initially generated particle locations to obtain the centroid errors in x-, y-, and z-directions. To obtain reliable statistical results, a large number of simulations have been performed.

The simulations indicate that, uncertainty in z-direction is indeed much more severe than that in x- and y-directions. In general, x- and y-direction uncertainty is about 0.5 ~ 1 CCD pixel distance, which translates into 2 ~ 4μm in our simulation. The z-direction uncertainty is approximately 0.2 pitch distance, or 18μm at a pitch distance of 100μm. Clearly, z-direction accuracy can be improved by reducing z-direction pitch; for example, the uncertainty drops to about 8μm at a pitch distance of 50μm. However, smaller pitch distance requires to process a larger quantity of image data. The uncertainties may also increase with the increasing particle density, because the chance of having agglomeration increases, which makes centroid extraction more prone to errors.

### 4.1.2  Particle Reconstruction by Edge Detection Method

A natural approach to retrieving a 3D particle image from the digital images would be to cluster those pixels whose intensities are greater than an appropriate threshold and whose locations are close to each other into one 3D particle image. However, this approach could produce false particles by leaving out isolated pixels unless the 3D image is concentrated within a small number of adjacent pixels. In our previous version of HPIV (Pu and Meng 2000), those false particles were not detrimental since they were not likely to have counterparts in double exposures and thus were subsequently dropped out during particle pairing. In particle diagnosis however, we need a more reliable method to extract 3D particle images. To this end a volume rendering technique was developed to replace pixel clustering to identify 3D particle images. The method extracts the continuous exterior surface of a particle image rather than checking which pixel belongs to which particle. Since it is based on edge detection, we refer to this method as the Particle Reconstructed by Edge Detection (PRED) method. The PRED method guarantees to detect all the above-the-threshold pixels that are connected and hence it preserves the 3D particle images much better than simple pixel clustering.

11

The first step in the PRED method involves the detection of the edges (2D boundaries) of particles in individual image planes. A proper threshold value is selected to convert a raw image into a binary image where pixels are classified into two categories: background and particle. As illustrated in Figure 8, assuming the search direction is clockwise on a binary image, a pixel on the right side of the edge curve belongs to the *"particle"* and the left side belongs to the *"background"*. All edges in an image can be found in this fashion and all edges are *"closed curves"*. After the edge detection all the pixels on and inside the boundaries are recorded for better accuracy in calculating particle centroids. This gives a more accurate centroid calculation but results in about 10 times more data than our previous pixel-clustering algorithm. Still, the data compression ratio is still over $10^3$ as compared to the raw image.

Once the 2D boundaries of particle images are extracted the next step is to collect them to form the 3D surfaces of the particles. It has to be determined whether two given 2D boundaries (either on the same plane or on adjacent planes) belong to the same 3D particle image. We set a simple criterion for this purpose. If, regardless of the z-coordinates, two adjacent 2D boundaries overlap with each other, they are considered to belong to the same particle image and therefore should be clustered, as shown in Figure 9a. At the first glance one might think that such a criterion may miss many 2D boundaries that are distinct on the same plane but belong to the same particle image. The key to avoiding such a problem is to use a recursive algorithm so that any two distinct boundaries will be clustered if they are connected with the same descendent 2D boundary down the search tree, as illustrated in Figure 9b. Hence, with this algorithm the search is guaranteed to travel through and record correctly every pixel enclosed in the 3D particle surface. In this way the full 3D particle image, no matter how complex, is preserved.

## 4.2 Concise Cross Correlation (CCC) algorithm

The essential part of CCC is the correlation, which will be discussed in detail first. Particle pairing after correlation will be discussed last.

Conventional FFT-based correlation has been the norm for velocity field extraction in planar PIV. For holographic PIV, where 3D velocity components are extracted in a 3D volume, it is generally assumed that this standard correlation method can be directly extended to 3D by either working with a 3D matrix [11][12] (Gray and Created 1993; Huang, K., *et al.*, 1993) or two stereo 2D matrices [1][2] (Barnhart *et al.* 1994; Meng 1994). Direct 3D FFT correlation appears impractical for high-resolution, large-volume off-axis HPIV measurement, since there are usually over 100 Gbytes of 3D image data per hologram, which, with FFT-based algorithms, can easily take thousands of hours to process. Furthermore, FFT-based correlation methods are effective only for high-density particle images and are thus prone to generating "bad vectors" in regions of low seeding densities [13] (Meinhart *et al.* 1995). Unlike the case of planar PIV, HPIV deals with 3D volumetric recording, where the high seeding densities required for successful FFT-based correlation are difficult to achieve at an acceptable signal-to-noise ratio due to speckle noise [4] (Meng *et al.* 1993). Hence, 3D FFT-based correlation is deemed unsuitable for our off-axis HPIV system. On the other hand, working with two stereo 2D matrices does provide relatively fast processing speed, but it suffers from an inherent low accuracy in

12

depth direction and, more critically, requires a large viewing angle of the hologram to fit in two cameras. This often imposes difficulties on the holographic scheme [2] (Meng 1994).

We recognize that since only the displacements of particle images or at most their locations carry the information needed for velocity field measurement, it is unnecessary to store and handle the entire image data (which include redundancies such as particle sizes, shapes, intensities, background conditions etc.). Hence a correlation procedure can be applied directly to the 3D locations of particles. This idea is implemented in the novel CCC algorithm, which yields a compression ratio of 4 to 5 orders and an increase in processing speed of 3 orders of magnitude.

The basic idea of CCC comes directly from the primary definition of cross correlation, whose physical meaning is image translation and multiplication/accumulation. Essentially, to cross correlate a group of particles in two exposures is to match the morphological patterns of the two images. The resemblance between the two patterns depends on the time interval between the two exposures and the velocity gradient of the flow. Therefore, the morphological deformation between the two patterns can be limited to an acceptable level by setting a small enough time interval. It is important to recognize that the correlation (pattern matching) procedure described above can be performed on particle centroid coordinates. Since most pixels in the acquired CCD image are dark background, the whole image data can be represented by a sparse matrix by taking all the particle centroids in the image as 1 and the background as 0.

The correlation works with two groups of particle centroids whose 3D coordinates are extracted from a pair of images in the double exposures. Keeping one of them fixed in its original place, we translate the other one in the 3D space and compute their correlation intensity. The displacement yielding the highest correlation peak is considered the displacement of the particle group and is the correlation output. Figure 10 illustrates how CCC works.

To quantify the probability of valid correlation results, or the "correctness", of CCC under various conditions, Monte Carlo simulations are performed. In correlating double exposures there are always particles in one group that do not have matching particles in the other group. We refer to them as "false" particles. Due to velocity gradients, the morphological patterns of the centroids also change between the two groups. The false particles and the morphological deformations are the major causes of invalid correlation. In the simulation we generate one group of centroids that are randomly distributed in a volume, then translate them by a given distance, individually shift each centroid by a small but random amount to mimic fluid deformation, and add a certain number of false particles to form the second group. Then CCC correlation is applied to these two groups of particles, and the correlation result is compared with the generated translation to validate the result. If the difference between the correlation result and the preset displacement is within one particle size, it is considered "correct".

Illustrated in Figure 11 (a) is the correctness of CCC as a function of the percentage of false particles. Performance under a wide range of densities (10 ~ 270 particles per IC) has been simulated. In most cases with as many as 40% false particles the validity is still

13

above 80%. Figure 11 (b) shows the correctness of CCC as a function of morphological deformation. In the figure deformation is indicated as percentage of IC size. It is found that satisfactory results can be obtained by CCC even at as high as 10% deformation.

After CCC finds the mean displacements of particle groups, individual particles are paired to give individual particle displacements or super-resolution. In each Interrogation Cell, the first set of particle centroids is shifted towards the second by the mean displacement calculated from CCC. Now that there is no net displacement of the particle group but only net deformation between the two exposures, if the deformation is within a limit (as usually required by PIV), pairing can be accomplishable on the basis of the closest distance. Out of one IC, this pairing process produces multiple vectors corresponding to individual particles, achieving higher resolution and accuracy beyond correlation results. Theoretically, pairing process can produce hundreds of vectors out of one IC in contrast to FFT-based approaches, which produce only one vector out of one IC. Nonetheless, actual gain in spatial resolution depends on seeding densities used and quality of holograms. Large translational displacements of particle groups also reduce the number of particles that can be paired since some of them leave the IC volume.

The key elements of HPIV data processing can be summarized as follows:

- *centroid finding* provides large compression of image data,

- *CCC (correlation)* gives particle group velocities efficiently and reliably, and

- *particle pairing* provides super-resolution in velocity field.

## 5   HPIV Accuracy

### 5.1   Accuracy of the PRED method

The PRED method used in our particle diagnostics experiment was validated with simulations using numerically generated particle images and its accuracy was quantified. Since it is difficult to predict the correct 3D particle intensity distribution for a given holographic system and alignment, it is unrealistic to expect to obtain meaningful tests of the PRED method by using real holographic experiments. Validation using simulated particle images appears to be a viable alternative. Simulations were performed for both 2D edge detection (to determine x- and y-direction accuracy) and 3D centroid detection (to explore z-direction accuracy). The analysis of the accuracy of 3D centroid extraction included two types of simulations: the first one to determine the error of the 3D centroid for a *single* isolated particle (which defines the upper limit of the accuracy) and the second one to quantify the accuracy of 3D particle centroids and velocities extracted from particles in a flow at a given particle density.

### 5.2   Accuracy of 2D boundaries and centroids

To evaluate the accuracy of the planar edge detection and centroid finding, computer-generated images were used. The test particles had diameters of 5, 10, 15, 20, 25 pixels,

14

and the entire image size was 1024x1024 pixels containing various numbers of particles as shown in Table 1. Since the domain size of the simulation was fixed, different particle numbers corresponded to different particle sizes. In each realization the number of particles was large enough to obtain stable statistics. The intensity of each 2D particle image was modeled by a Gaussian distribution. A typical edge detection and centroid finding example for an image plane is shown in Figure 12. The white curves around particles are edges detected, the black crosses at the centers of particles mark the calculated particle centroids, and the gray parts within the edges represent the binary form of the *original* particle images. The image shows that the edge detection was successful since all the detected edges coincide with the true edges.

The statistics of the 2D centroid finding error can be determined from the simulation results. Since the true centroids of these particles are known, we can compare the retrieved centroids with the true ones. The errors are recorded in Table 1. The table shows that the mean errors of the centroid finding for all tested particles sizes are around 1 pixel, which is the limit of what can be resolved in an image.

## 5.3 Accuracy of the 3D centroid of a single particle

In the simulation of a single 3D isolated particle, a modeled 3D particle image was generated and projected onto 50 consecutive image planes (the plane size was 128×128 pixels, corresponding to 0.5mm×0.5mm) equally spaced at a pitch distance of 40μm in a volume. For simplicity the distribution of particle image intensity was modeled by a Gaussian distribution:

$$\text{Error! Objects cannot be created from editing field codes.} \tag{5}$$

where x, y, and z are the coordinates relative to the focal point of the particle image, $I_0$ is the center intensity at the focal point, $r_0$ is the size of the particle, and $\alpha$ is the angular aperture of the particle image determined from the exposed hologram area and the distance from the particle to the hologram. The effective edge of the image section varies along the z-axis hyperbolically. This variation is schematically illustrated in Figure 13. White noise, with the intensity randomly ranged from 0 to 50 on a scale of 256, was added to all the pixels in the image to simulate holographic noise. Different particles of sizes ranging from 10 to 50μm were simulated. Shown in Figure 14 was a single simulated particle image (30μm in diameter) on selected planes separated by 100μm along z direction. Such a modeled particle image was used to examine the effectiveness of the PRED method. Despite its simplicity the model with added noise captures some critical aspects of the real 3D image such as varying intensity along the depth and possible splitting of the image.

The results of the single particle simulations show that the particle size did not significantly affect the absolute error of a single particle centroid (the variation was less than 1μm). The average centroid error was approximately 3.2μm. This centroid extraction accuracy on a single particle sets the upper limit for what we can accurately measure using the HPIV technique.

...parison, we also tested the accuracy of the 3D centroid for a *single* isolated ... the previous pixel clustering method [8] (Pu and Meng 2000). The average ...out 4.8µm, compared to 3.2µm for the PRED method. Here, the difference ... icant since the image was modeled by Eq. (5) with no "fingers" and the ... clustering of particles was not captured.

### ...racy of 3D particle centroids and displacements in a flow

In the simulations of a group of particles dispersed in a known flow, two groups of particles of 15µm diameter were generated. The second group was transformed from the first according to a spiral motion. Figure 15 shows the simulated spiral motion – a solid-body rotation at an angular speed of $\omega$ about an axis oriented at ($\theta$, $\phi$) (where $\theta$ and $\phi$ are arbitrary angles) plus a translation $s$ along the rotation axis. Digitally generated particles using Eq. (5) were randomly dispersed in the 3D space to follow the spiral motion of the simulated flow. The image volume was then scanned plane-by-plane along the z-axis. The IC size employed in the simulation was $2\times2\times2$ mm$^3$, $\phi$ was set to 0, and two z-direction pitch distances, 50 and 100 µm, were tested.

The simulated 3D dispersed particle image field incorporated both the effect of individual particle intensity distribution (albeit simplified) to allow centroid finding to be tested, and the effect of drastic velocity gradients to allow the CCC algorithm to be validated. We applied the entire HPIV data processing procedure to this simulated particulate flow and extracted both centroids and displacements of the particles. Although the PRED method has been shown by the single particle simulation to be better than the pixel-clustering for the images modeled using Eq. (5), here for the multiple particle numerical experiments the pixel-clustering algorithm was sufficient in testing centroid extraction and the CCC algorithm thus lowering computation cost.

Figure 16 shows a snapshot of the extracted 3D particle centroids and velocities from the simulated images, where gray and black dots represent particle centroids extracted from the first and second exposure, respectively. This extracted particle field was compared with the simulated particle field and the errors were determined. The spiral motion of the particles is evident from the processed velocity data. For a reliable assessment of the centroid uncertainties and the velocity mapping errors, a large number of simulations with various $\omega$ and $s$ values at different particle densities $N$ were performed so as to obtain the statistical distributions of the measurement errors.

Due to the sparse spacing of image acquisition planes the errors for the centroid location in the z direction ($\delta_z$) were much larger than those in x and y directions ($\delta_x$ and $\delta_y$). Figure 17 shows the probability distribution of $\delta_z$ for two values of z-direction pitch distance $d_p$. The distribution of $\delta_z$ at $d_p = 100$ µm spans much wider than $\delta_z$ at $d_p = 50$ µm. It is clear that the 50µm pitch distance overall gives much smaller $\delta_z$ than the 100µm distance. Shown in Figure 18 are the mean centroid errors $\overline{\delta}$ for the x-y plane and the z direction as a function of the particle density. Again, it is apparent that the error along z strongly depends on the pitch distance. The slight increase of the uncertainties with the increasing particle density can be attributed to the increasing chance of agglomeration of images. Figure 19 shows the mean error of the particle displacement, $\varepsilon$, in the spiral flow

16

as a function of the particle density. From Figure 18 and Figure 19 the displacement error is slightly lower than the centroid error, which is a result of a strict culling process (*i.e.* a centroid with a larger positional error is less likely to be paired, and it is therefore less likely to be included in the final result of the extracted particle displacement).

It seems sensible that the pitch distance should be further reduced to achieve higher accuracies along the z-direction. However, the pay-off may not be significant due to the finite depth of focus in the particle images and the increase in the data acquisition and processing time. The complete processing of a typical hologram in our off-axis HPIV system took about 7 hours with the pixel-clustering method implemented on a single PC. With the PRED method, it is estimated to take 3 times longer.

## 6   Experimental Results

### 6.1   HPIV measurement of a vortex ring in air

The off-axis HPIV system described above has been tested with measurement of a forced jet. Depicted in Figure 20 is the experimental setup for the measurement of the vortex ring. The airflow, generated by a miniature electric fan, is seeded with water droplets 5μm in size. It enters a chamber with a loud speaker mounted on the bottom and passes through a honeycomb, a contraction, and a circular nozzle. At 1-in. downstream of the jet exit, a vortex ring is formed, which travels at ~ 2m/s, corresponding to Re ~ 3400. The acoustic forcing is synchronized by a Phase Locked Loop (PLL) with the 10Hz laser pulses at constant (adjustable) phase delay, producing a stationary vortex ring located in the center of illumination. The dispersion of droplets in the 3D vortex ring is rather inhomogeneous, and the propagation of the vortex ring is unstable, as illustrated in Figure 21 (a) and (b). The average seeding density in the vortex ring is approximately 30 particles per mm$^3$, which produces excellent image quality for data processing.

The R-O intensity ratio used to record the hologram is approximately 4:1. Depth of focus of particle images in this experiment ranges from 0.3 mm to 0.5 mm, for which a pitch distance of 100 μm is chosen for depth interrogation. A 4× microscope objective lens is mounted on the CCD camera to obtain a 2×2 mm viewing area, and with 20 image planes in each IC, the IC size is 2×2×2mm. Therefore in the whole image volume, 50 (width) × 40 (height) × 50 (depth) = 12500 interrogation cells are acquired and processed, containing 250000 planar interrogation spots. With the CCD resolution of 1k x 1k, this corresponds to 250 Gbytes of data, which took approx. 50 hours to process at the time of this measurement in 1997 (the speed has since increased by 7 times).

Shown in Figure 21 (c) are coarse 3D vector map in the flow volume extracted with CCC algorithm (correlation only). This instantaneous 3D snapshot of the test flow consists of approximately 6000 vectors. Only about 5% of the vectors produced by CCC are bad vectors, which can be easily identified and eliminated based on their lower correlation peak values. After cleanup of bad vectors, the residual bad vectors are well below 1%.

The 3D vortex ring structure can be identified from this preliminary 3D vector map. To increase spatial resolution, particle pairing is further performed on individual particles using the average vectors generated by CCC as references. More than 92,000 vectors are produced after particle pairing, gaining 15 times higher spatial resolution. The resulting raw velocity field is shown in Figure 22, where the vectors are irregularly distributed in the 3D space. Since the particle distribution is inhomogeneous, at some test points there is no data.

From the dense version of the 3D velocity vector field, 3D vorticity field is calculated. To deal with missing data points and achieve higher accuracy, the velocity vectors are interpolated on a regular grid prior to the vorticity calculation. Illustrated in Figure 23 is a vorticity iso-surface created from the computed vorticity field. It clearly depicts the 3D topology of the vortex ring measured.

## 6.2    HPIV measurement of a tab wake in a water channel

To test the feasibility of the HPIV measurement for water flows, off-axis HPIV technique is applied to a water channel flow with a tapered passive mixing tab mounted on the wall. The wake of such a tab is known to produce complex 3D vortical motions including a series of hairpin vortices [14][15][16] (Yang et al. 1998; Yang & Meng 1999; Gretta & Smith 1993) and thus the tab is often called vortab. The free-stream flow velocity is approximately 16.7cm/s, corresponding to Re ~ 12,000 based on the channel height and 2080 based on the tab height.

The holographic recording geometry of this flow is depicted in Fig. 11. The optical configuration is similar to the one employed in the air jet measurement. Hollow glass beads sized around 9μm are illuminated by the volumetric laser beam at the test section. In this experiment, higher processing speed is achieved by adopting a large aperture objective lens with a low magnification. As a result the camera viewing area (and IC size) is increased to 4mm×4mm and the processing time is reduced to 7 hours.

Figure 2 shows a 3D snapshot of the velocity field measured in a volume of 44mm × 56mm × 32mm composed of 9856 ICs. Around 80,000 paired vectors are produced, which is about 50% of the total number of particle centroids extracted. The low percentage of pairing is due to the large displacement between two exposures. The paired vectors are gaussian-interpolated onto regular grids at 0.6mm×0.6mm×0.6mm spacing, resulting in approximately 400,000 vectors. The gaussian radius used in the interpolation is 75% of the IC size. For clarity only those vectors on the outer surfaces are plotted, and the mean velocity averaged over all the vectors in the volume has been subtracted to make velocity gradients more visible. In the figure part of the volume is cut off to show the internal vortices. Coordinates X, Y and Z denote streamwise, wall-normal and spanwise directions, respectively. From this 3D velocity field, instantaneous vorticity field is computed to identify the hairpin vortex structure found in this flow using PIV [14][15] (Yang et al. 1998; Yang & Meng 1999) and flow visualization [17] (Elavarasan & Meng 1999). Shown in Fig. 13 is an iso-surface of the vorticity field, where three hairpin vortices are identified in the 3D volume. Their size and streamwise spacing match those found by [14] Yang et al. (1998). Such *instantaneous* 3D vortex structures,

represented by vorticity magnitude, were only obtainable through numerical simulations before HPIV. The only other instantaneous 3D vortex structure obtained from experiments is an unstable vortex ring recorded with HPIV [7] (Meng & Hussain 1995b).

## 6.3  Result Validation

The measurement accuracy of HPIV largely depends on the data processing. We have conducted a series of simulations to study the contributions of these factors. In this paper, however, we restrict our discussion to an evaluation of the accuracy of our experimental results described in section 6.2 HPIV measurement of a tab wake in a water channel.

At first we examine what ultimately limits the velocity accuracy. Since the velocity field in Figure 2 is derived from paired particles, *i.e.* the connection of particle centroids, uncertainty in centroid locations is the defining factor to measurement accuracy. During the data acquisition in this experiment, a plane pitch distance of 100 μm is employed. As mentioned in Section 4.1, this produces an uncertainty of approximately 18μm in particle centroid. The mean displacements of particles extracted from the hologram are approximately 247μm, or 61 pixels in the digital image plane (corresponding to a mean velocity of 16.5cm/s with the double-exposure time interval of 1.5ms used in the experiment). Therefore we estimate an overall velocity accuracy of no better than 7.3%.

Further validation of the experimental data is accomplished through examination of continuity equation. First, from the measured 3D velocity field, $\nabla \cdot \mathbf{u}$ (theoretically zero for the incompressible flow) is computed based on finite difference, whose Probability Density Function (PDF) is depicted in Figure 24. It is found that the divergence has a mean value of $0.51s^{-1}$ and a standard deviation of $6.63s^{-1}$. The absolute value of divergence $|\nabla \cdot \mathbf{u}|$ has a mean value of $5.11s^{-1}$ and 95% of data points are within divergence absolute value of $12.9s^{-1}$.

To provide a relative measure of error, we further resort to the mass conservation over an arbitrary control volume $CV=\Delta x\Delta y\Delta z$. The net flux entering the control volume is

$$\Delta Q = \iiint\limits_{CV} \nabla \cdot \mathbf{u}\, dV \ . \tag{2}$$

To estimate the order of the net flux, we introduce a characteristic velocity $U$, which is the main flow velocity in the flow field. The total flux passing through the control volume can be estimated as

$$Q = U \cdot \Delta y \Delta z \tag{3}$$

Therefore the non-dimensional ratio

$$\eta = \frac{\Delta Q}{Q} \tag{4}$$

provides an excellent indication of how well the continuity equation is satisfied.

For an estimation of the worst case, we choose the 95% coverage divergence value and the smallest control volume size (the grid size). In this case $\Delta Q$ is circa 2.78mm³/s. On the other hand, the mean flow velocity can be chosen as the characteristic velocity and

$Q$ is estimated to be around 59.0 mm$^3$/s. Therefore we estimate $\eta \sim 4.7\%$. Hence, continuity is satisfied reasonably well.

# 7  Discussion

A Holographic PIV system has been developed with support in part from the Air Force Office of Scientific Research under grant number (F49620-98-1-0414). HPIV is now recognized as a viable next-generation full field (3D) particle diagnostic technique. With full 3D instantaneous particle velocity information complex flow geometries can be investigated to provide invaluable insight into and validation of the fluid dynamics. Further developments beyond the scope of this investigation have extended the technique to include densely particle laden flow diagnostics. The next phase of development will extend the technique to include temporal resolution approaching that of current 2D PIV instruments.

## Acknowledgements

# Figures



(a)



(b)
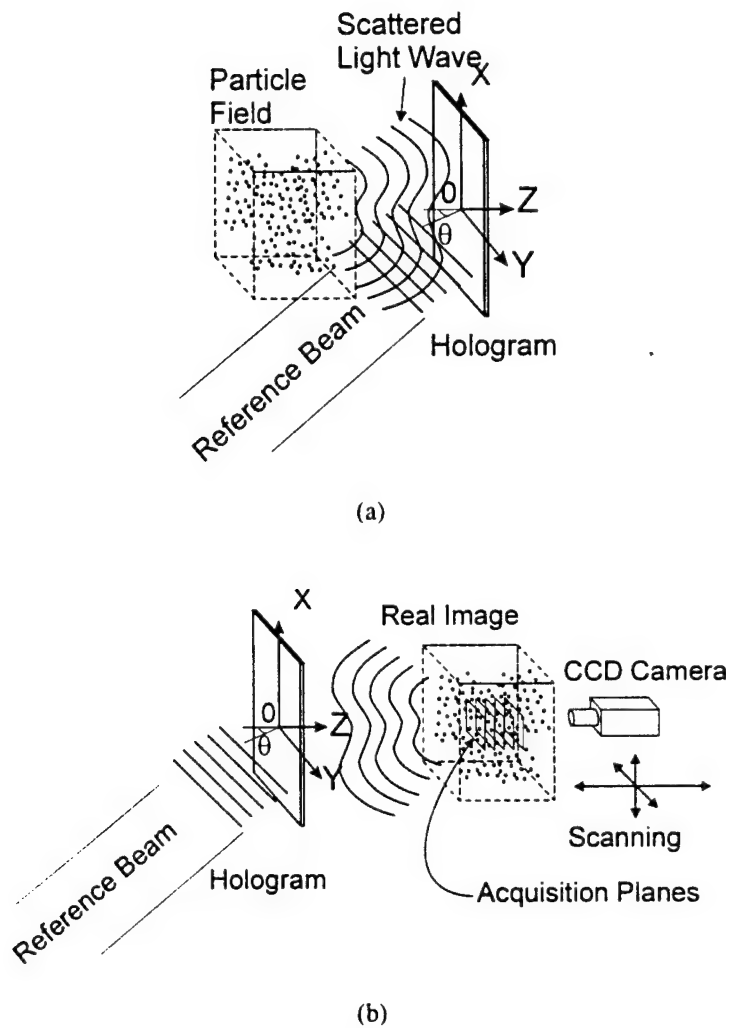
Figure 1: Principle of holographic diagnostics of a 3D particle field. (a) Hologram recording; (b) Hologram reconstruction. Illustrated scheme is off-axis holography. The virtual image wave and the direct transmitted wave during reconstruction are not shown.
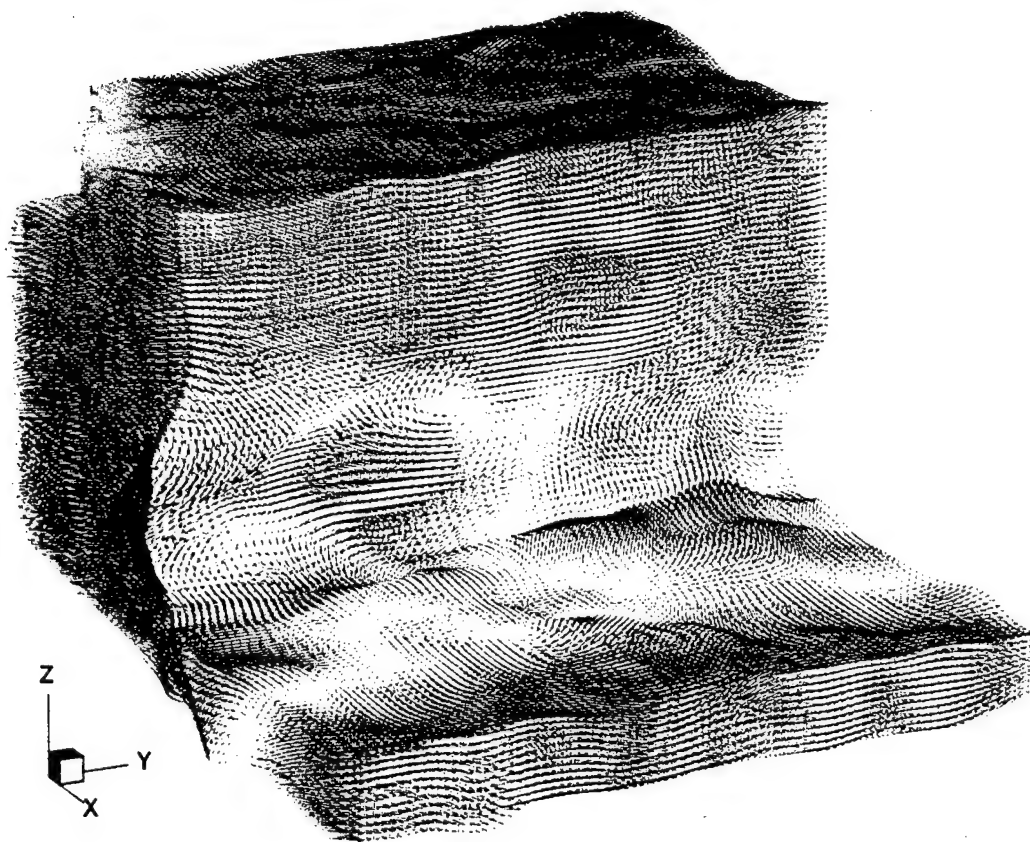
Figure 2 HPIV measurement of flow passing a trapazoidal mixing tab
mounted in a water channel flow, showing hairpin vortex structures. The
instantanous 3D velocity field is found to satisfy the continuity equiation
rather well.
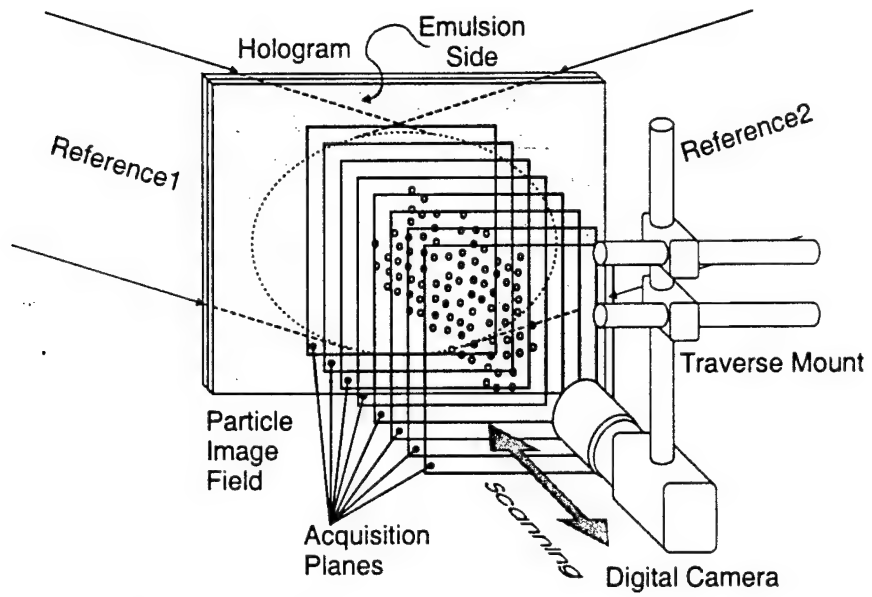
Figure 3 The off-axis HPIV system: Perspective view of the hologram in reconstruction and image acquisition by digital camera.
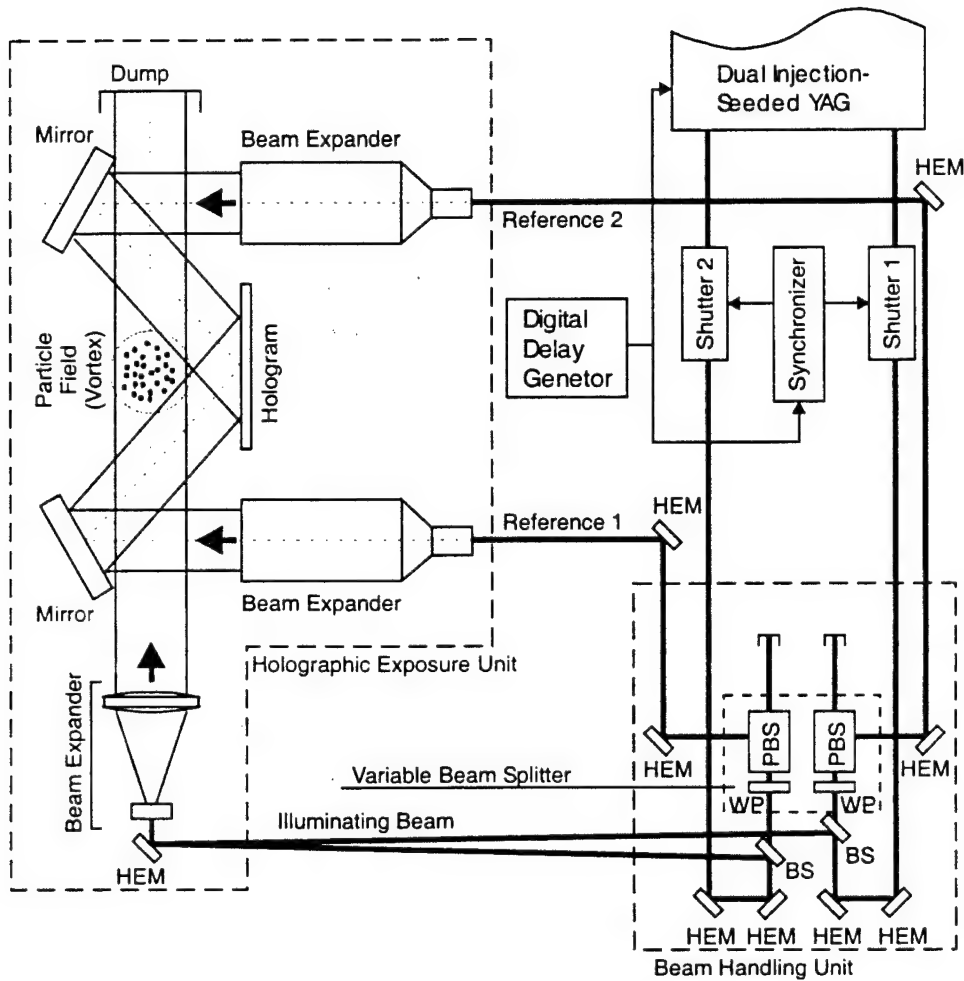
Figure 4 Schematic of off-axis HPIV recording. Two laser beams from the injection-seeded dual YAG laser, separated by a short time interval, are split by the beam handling unit into 3 beams: The illuminating beam, reference 1 and reference 2. The holographic plate is placed with the emulsion side facing the particle field. A 3D region of the particle field is illuminated, and their 90-degree scattering is recorded on the hologram. BS- Beamsplitter, HEM- High Energy Mirror, PBS- Polarizing Beamsplitter, WP- Waveplate.
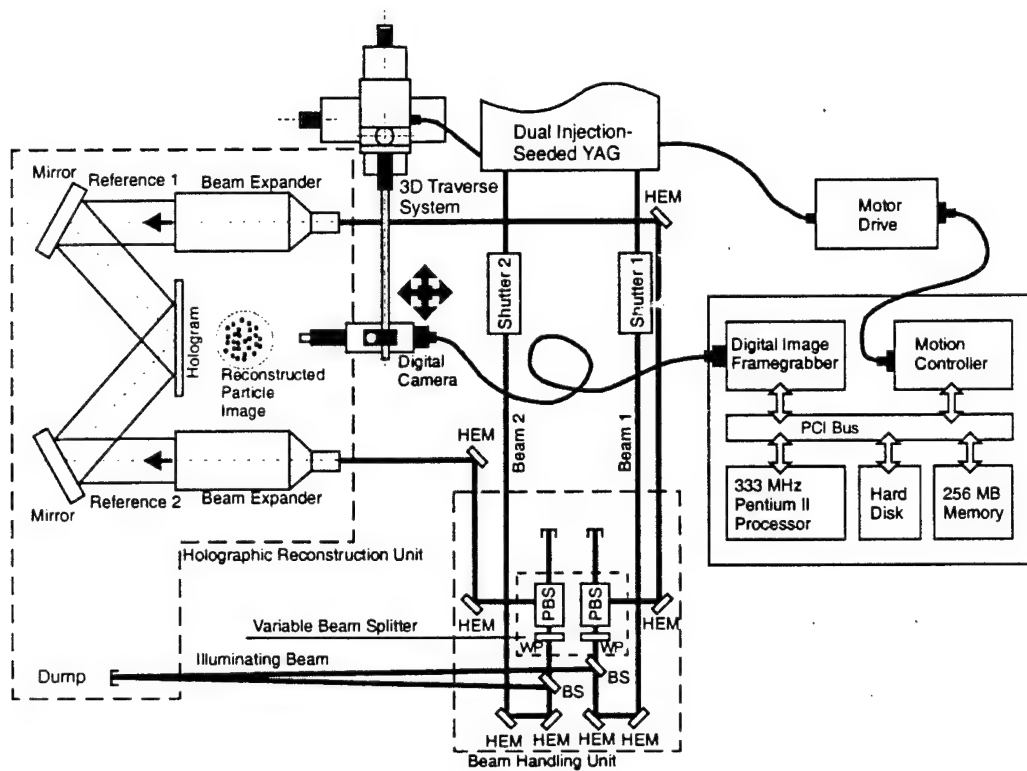
Figure 5 Schematic of off-axis HPIV reconstruction (*in situ*). The hologram is placed at the original location where it is recorded, albeit with emulsion side facing opposite to the reference beam, forming a real image of the particle field on the opposite side. A computer controls the traversing system to move the digital CCD camera in three directions and acquire images plane by plane.
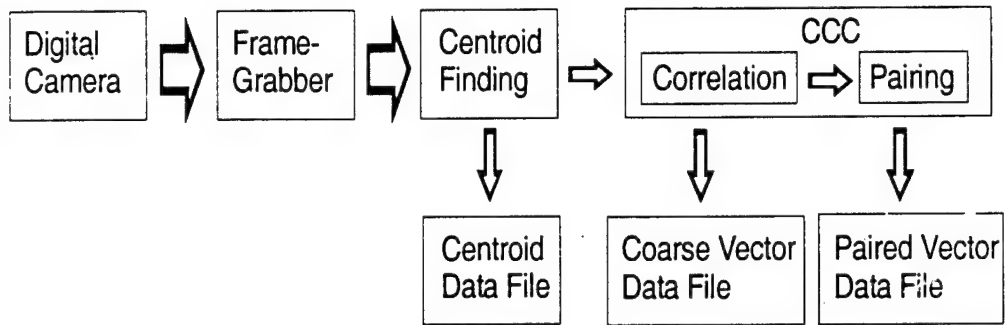
Figure 6 Data flow chart during HPIV data processing with Concise Cross Correlation (CCC) and particle pairing.



(a)



(b)
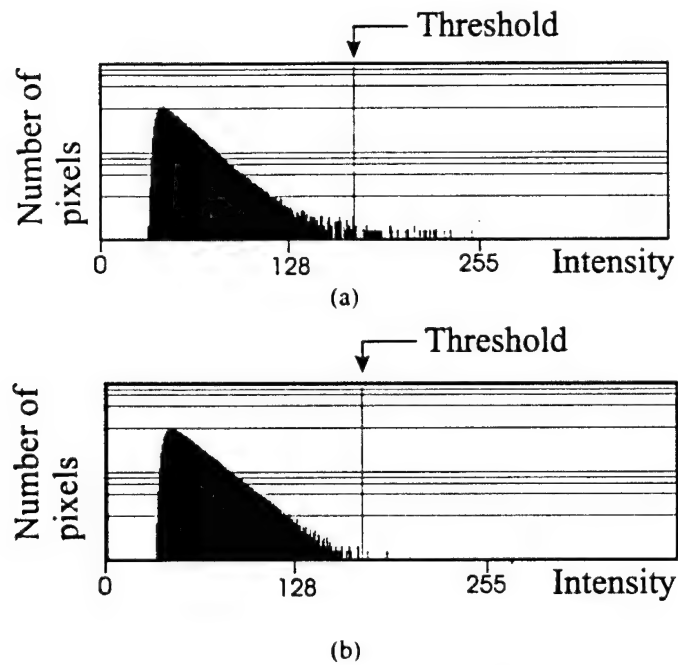
Figure 7: Intensity histogram of one acquired image plane in a logarithmic scale. (a) With particle images. There is a small peak at a high intensity value (255). Throughout the entire image volume, the percentage of pixels in such a peak is roughly constant. (b) Without particle images. The peak is absent.

| Edge | Inner pixels |
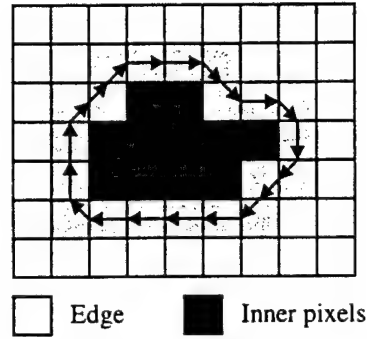
Figure 8 Edge detection for 2D particle image. Arrows on the edges show the search direction.



(a)

(b)
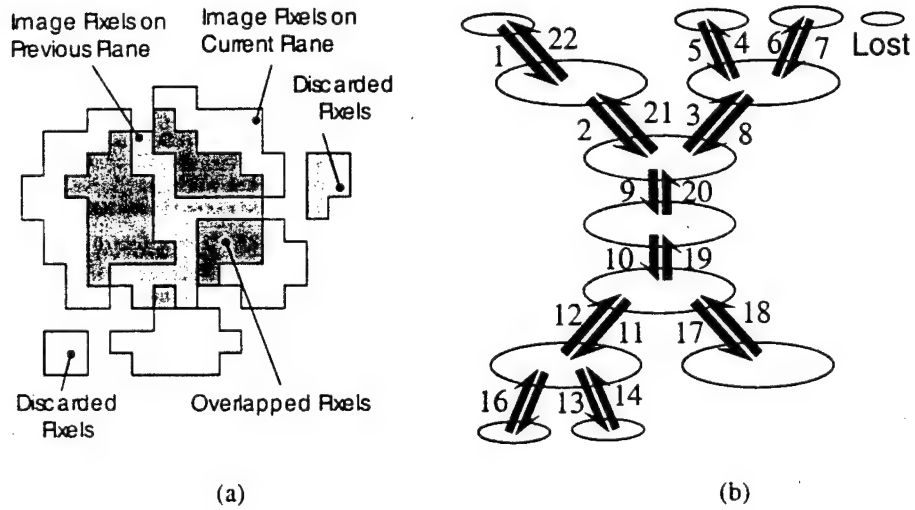
Figure 9 The PRED method for particle extraction. (a) Clustering criterion. If two 2D boundaries on two adjacent planes overlap, they are grouped as parts of the same particle. (b) The recursive collecting algorithm. The algorithm collects all the 2D boundaries that overlap with each other to form one 3D particle image.

(a)

(b)
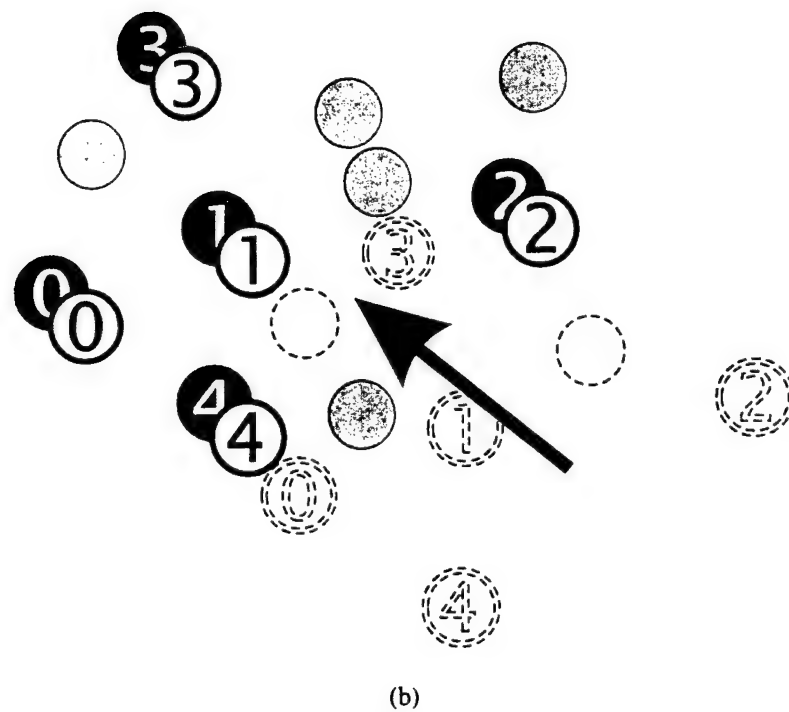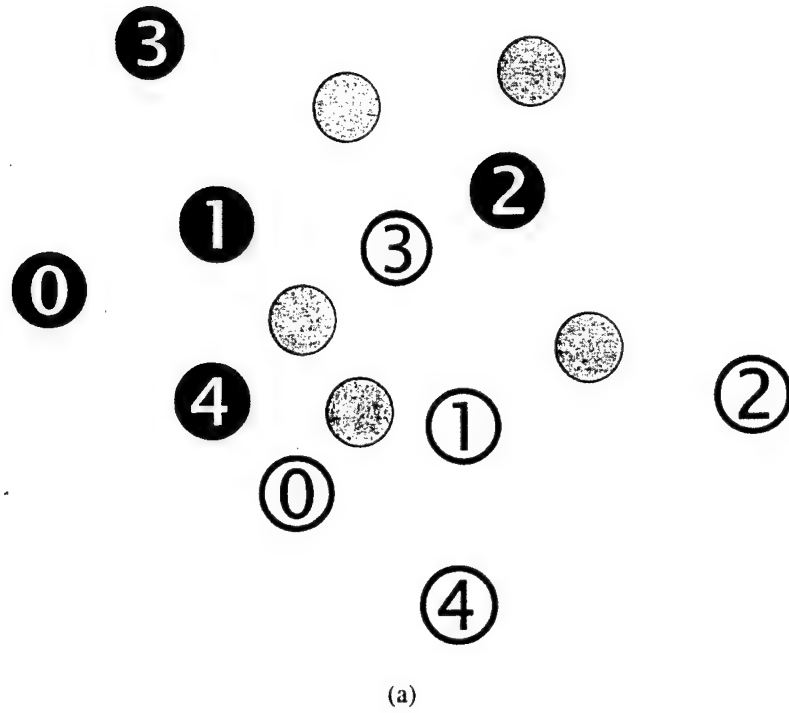
Figure 10 Principle of Concise Cross Correlation (CCC). (a) Black and white balls represent two groups of particle centroids corresponding to two exposures. For illustration purpose they are numbered. Gray balls represent noise. (b) During the calculation, white balls and some of the gray balls are translated in 3D space, until their morphological pattern best matches that of the black balls.
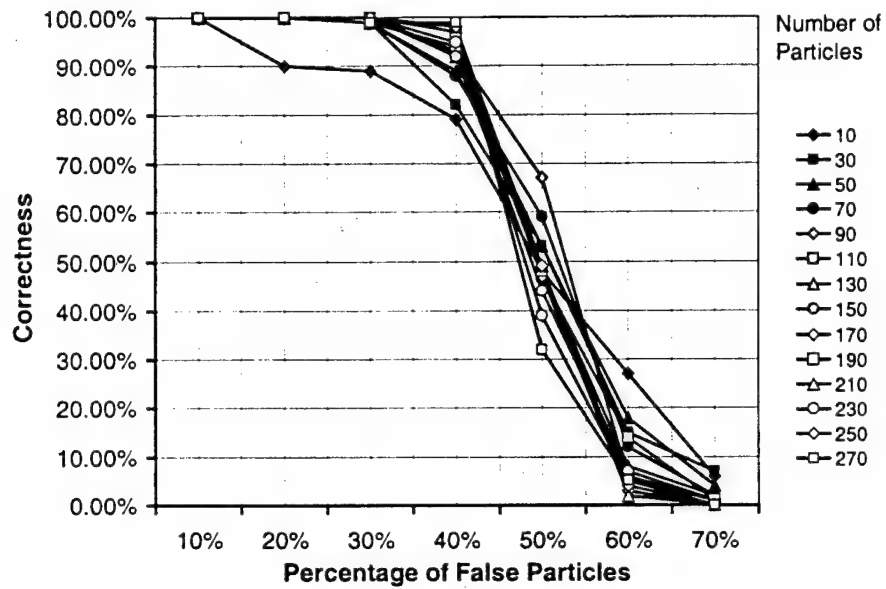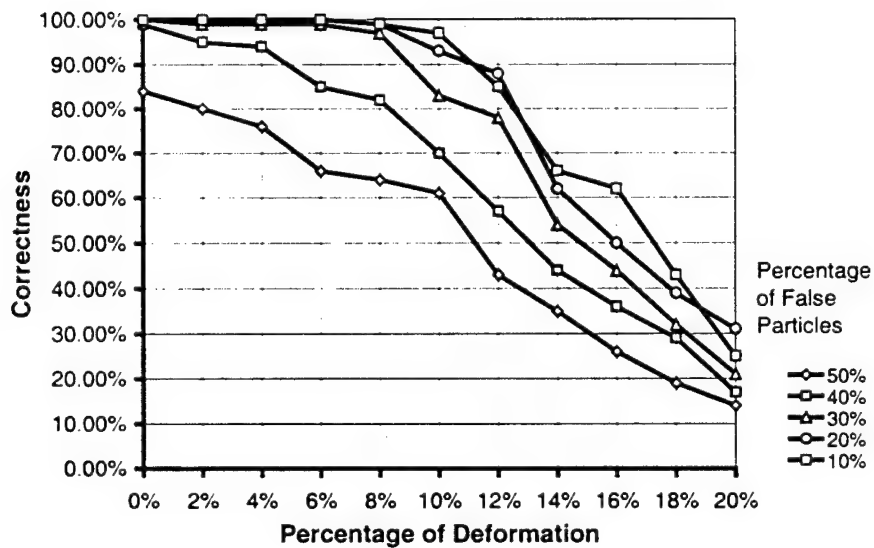
Figure 11: Correctness of CCC algorithm tested by simulation: (a) Correctness vs. percentage of false particles (noise) for various numbers of particles in a group. Average deformation is 2%. Note that with as much as 40% false particles the validity still reaches 80%. (b) Correctness vs. the amount of morphological deformation of the particle group for various percentages of false particles. The deformation is represented as percentage of the IC size.

29
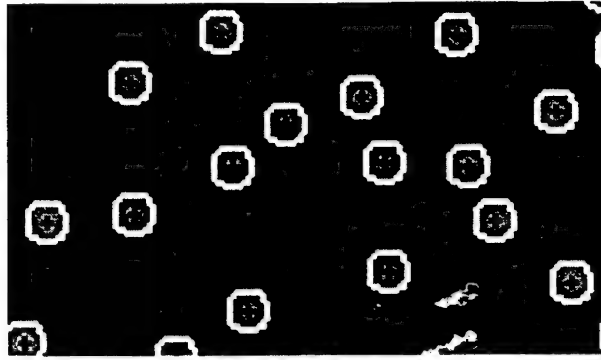
Figure 12: The zoomed-in image after 2D edge detection and centroid finding on simulated 2D particles.
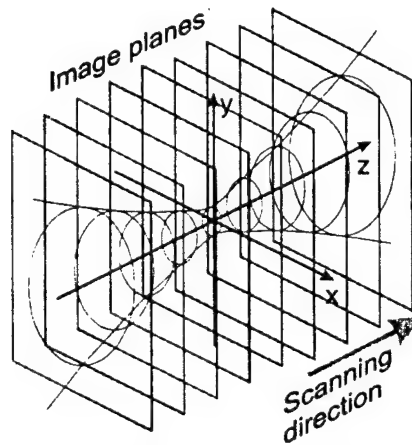


Figure 13: A simplified model of a 3D particle image distribution for testing the PRED method, centroid extraction, and the CCC algorithm. Noise (not shown) is added.



Figure 14: A simulated single particle image (30μm) on selected planes (separated by 100μm along z). The image area shown consists of 32×32 pixels.
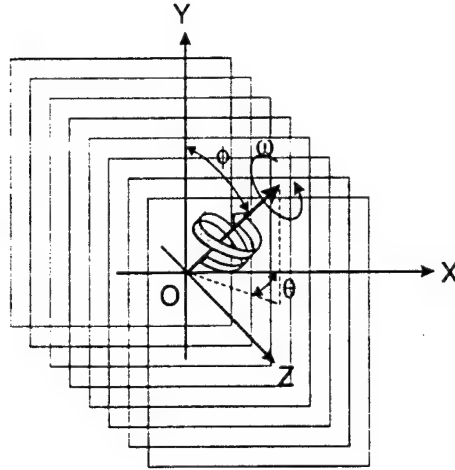
Figure 15: Geometry of the simulated spiral motion flow. Digitally generated particles are randomly dispersed in 3D space to follow the spiral motion. The volume is then scanned plane by plane along z-axis.



(a)                              (b)                              (c)
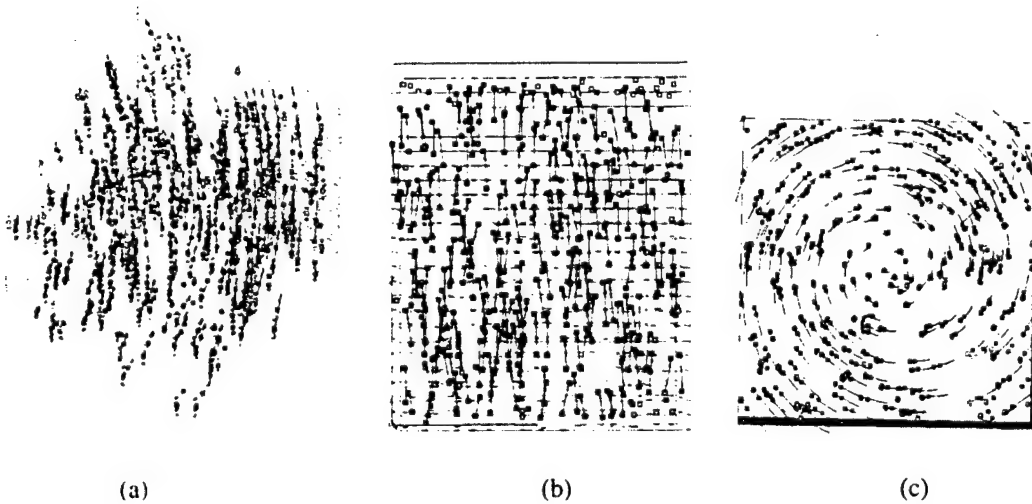
Figure 16: Particle centroids and velocities extracted from the simulated particle field in a spiral motion for $\phi$=0. Gray and black dots represent particle centroids in each exposure. The arrows indicate velocities. (a) Perspective view. (b) Side view. (c) Top view.
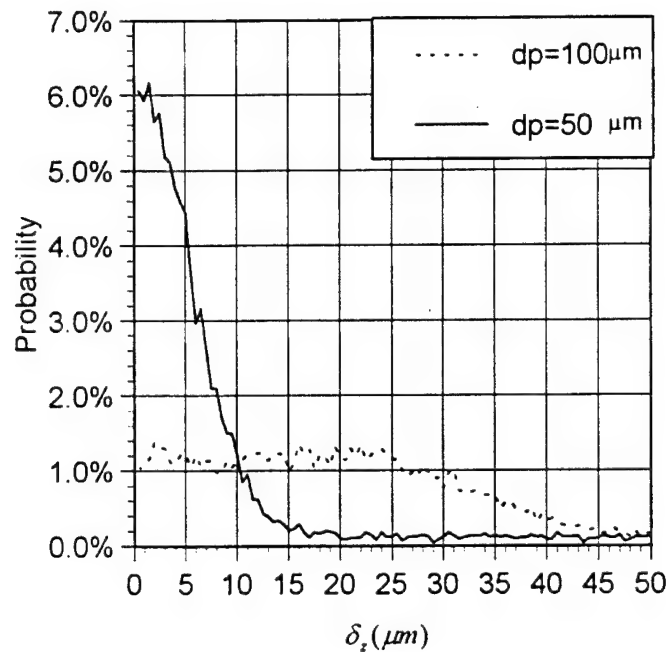
Figure 17: Probability distribution of centroid error $\delta_z$ for two z-direction pitch distances ($d_p$). Note that $\delta_z$ for $d_p = 100$ μm spans much wider than $\delta_z$ for $d_p = 50$ μm.
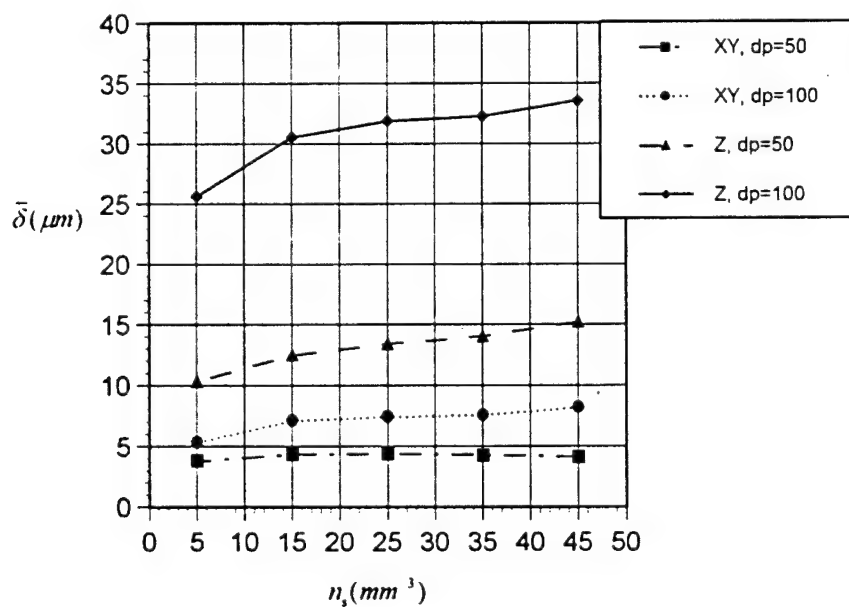


Figure 18: Mean centroid errors ($\overline{\delta}$) for the xy plane and the z direction versus the particle density ($n_s$) for $d_p$ for 50μm and 100μm. The pitch distance $d_p$ affects the z accuracy drastically.
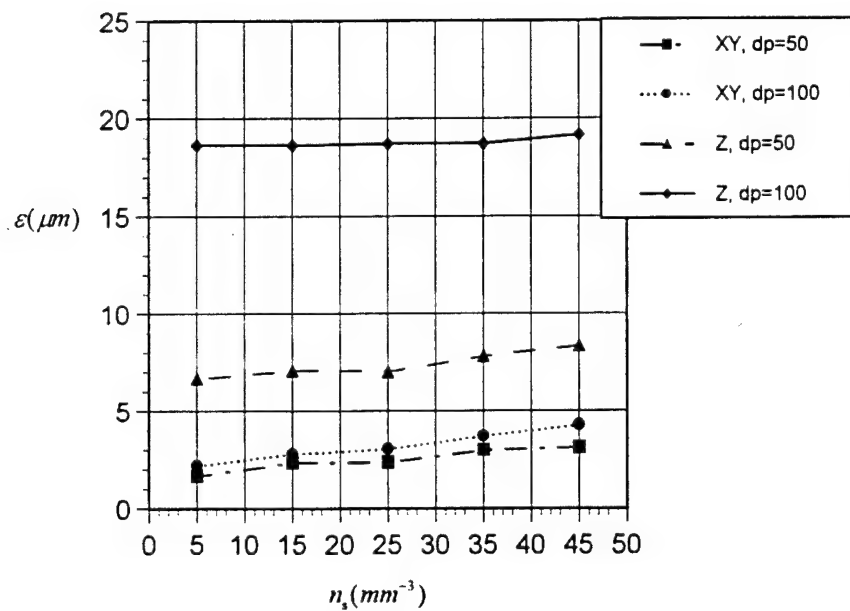
Figure 19: Mean displacement errors ($\varepsilon$) for the *xy* plane and the *z* direction versus the particle density ($n_s$) for $d_p$ for 50μm and 100μm.
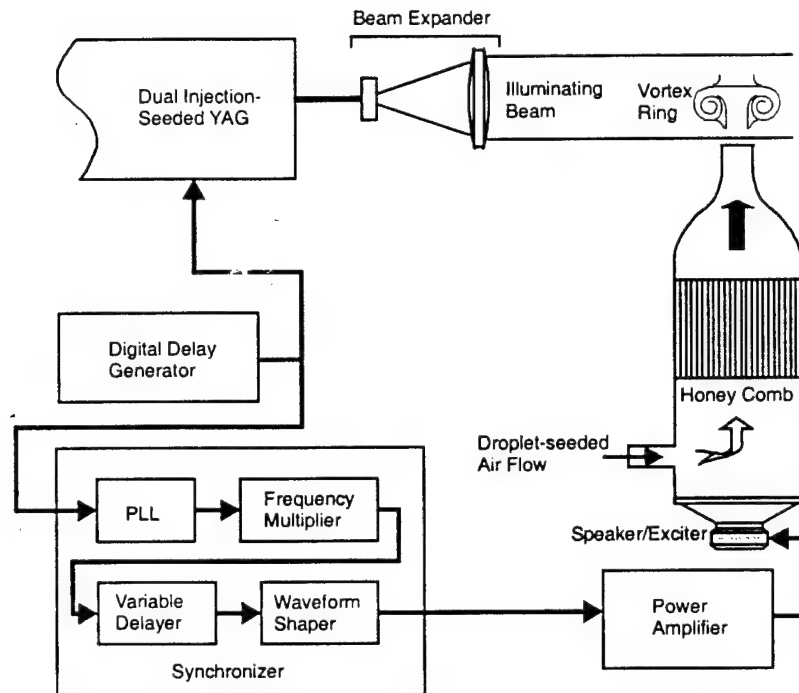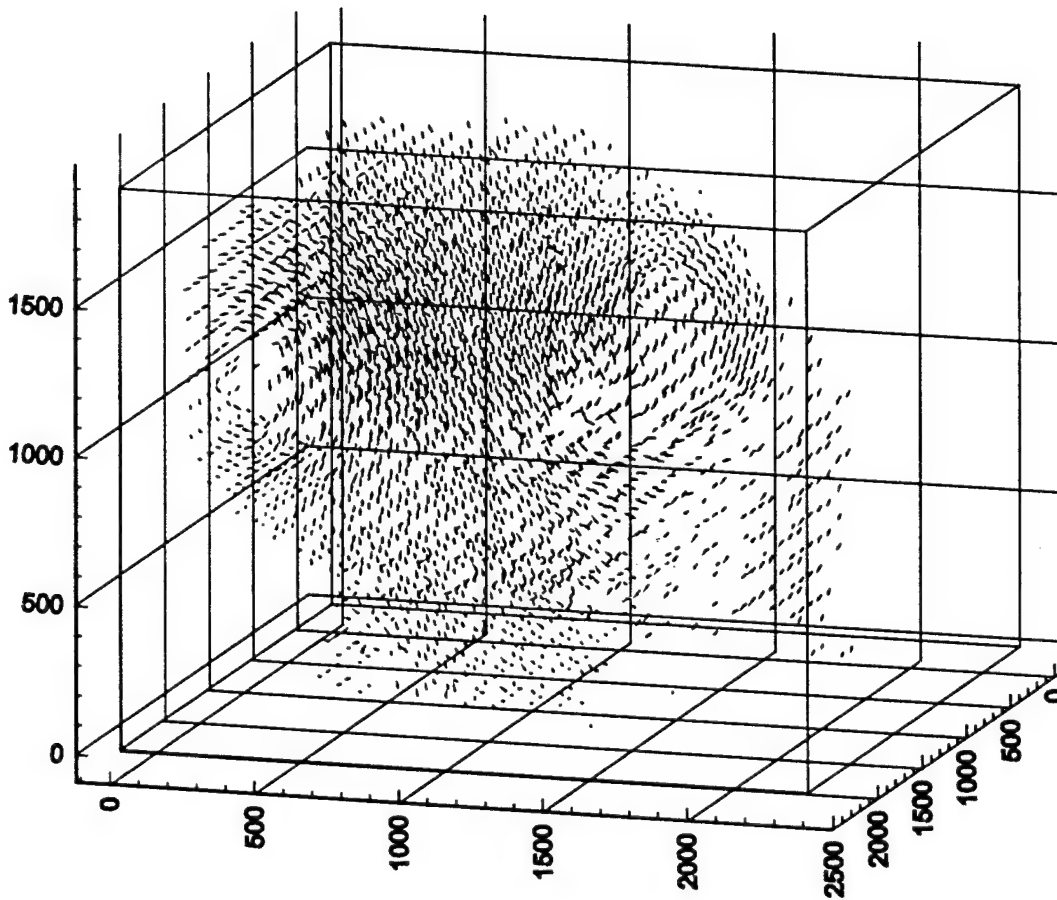
Figure 20: Recording of a vortex ring in an air jet. The vortex ring is generated from an acoustically excited jet and synchronized with the laser pulse.
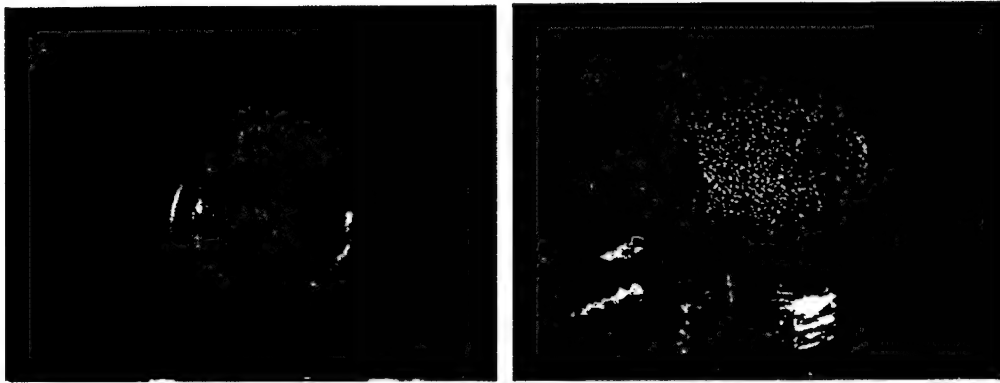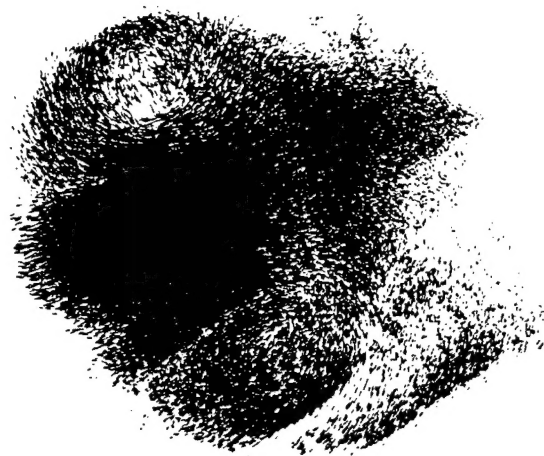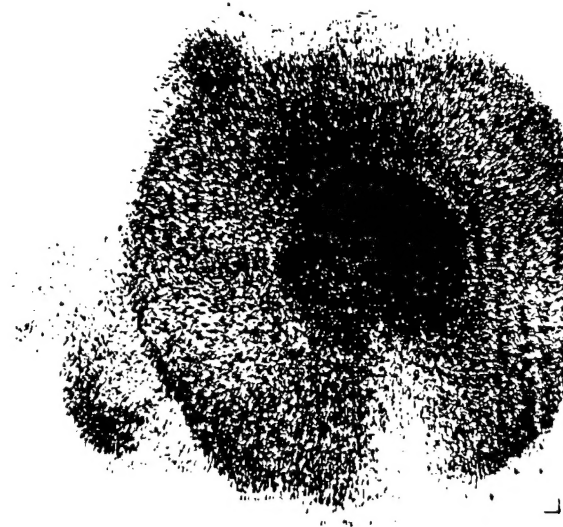
(a)

(b)

(c)

Figure 21: 3D vortex ring measured with HPIV. (a) and (b): side view and top view photography. (c) Coarse 3D velocity vector field extracted from the hologram by CCC before particle pairing. Mean velocity of the jet has been subtracted from the result.

(a)



(b)

Figure 22: Detailed 3D velocity vector field after particle pairing: (a) side view. (b) top view. Approximately 92,000 velocity vectors are inhomogeneously distributed. A velocity vector field on a regular grid can be generated from this data by interpolation.
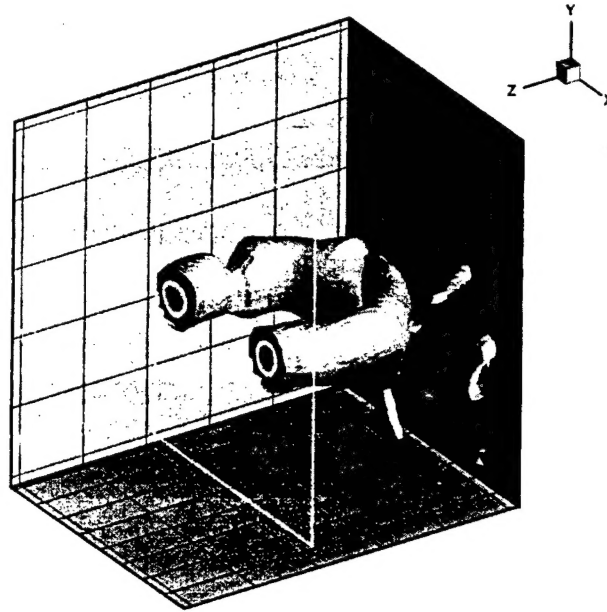
Figure 23: Vorticity iso-surface calculated from the 3D velocity field of the vortex ring shown in Figure 21. Part of the vortex ring is cut out to show the vortex core.
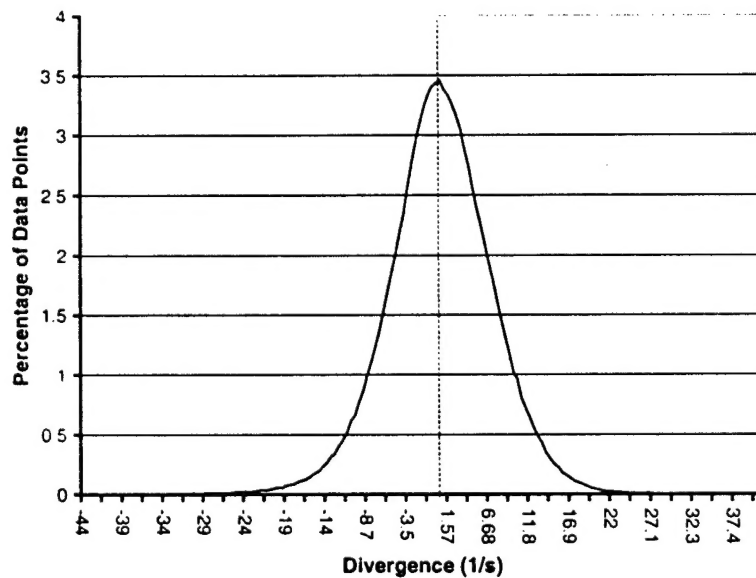


Figure 24: Probability Density Function of divergence calculated from the 3D velocity field shown in Figure 2. The mean of divergence is $0.51s^{-1}$ and its standard deviation is $6.63s^{-1}$.

# Tables

Table 1: Errors of calculated centroids by 2D edge detection and centroid finding

| Particle diameter (pixels) | 5 | 10 | 15 | 20 | 25 |
|---|---|---|---|---|---|
| Number of particles | 929 | 918 | 913 | 723 | 463 |
| Maximum error of centroid (pixels) | 1.36 | 1.52 | 1.55 | 1.70 | 1.82 |
| Mean error of centroid (pixels) | 0.76 | 0.90 | 0.95 | 1.10 | 1.17 |
| Standard deviation of centroid (pixels) | 0.28 | 0.29 | 0.28 | 0.29 | 0.30 |
| Relative maximum error of centroid | 0.2729 | 0.1521 | 0.1032 | 0.0849 | 0.0727 |
| Relative mean error of centroid | 0.1517 | 0.0903 | 0.0636 | 0.0548 | 0.0467 |
| Relative standard deviation of centroid | 0.0564 | 0.0286 | 0.0187 | 0.0144 | 0.0120 |

# References

1 Barnhart DH; Adrian RJ; Meinhart CD and Papen GC (1994): Phase-conjugate holographic system for high-resolution particle image velocimetry. Appl. Opt. 33: 7159-7169.

2 Meng, H. 1994, Development of Holographic Particle Velocimetry Techniques for Three-dimensional Vortical Flows, Ph.D. thesis, University of Houston, Houston, TX.

3 Zhang J; Tao B and Katz J (1997): Turbulent flow measurement in a square duct with hybrid holographic PIV. Exp Fluids, 23: 373-381

4 Meng, H., Anderson, W. L., Hussain, F., and Liu, D. 1993, Intrinsic speckle noise in in-line particle holography, J. Opt. Soc. of Am 10 pp. 2046-2058.

5 Jones AR; Sarjeant M; Davis CR and Denham RO (1978): Application of in-line holography to drop size measurement in dense fuel sprays, Appl. Opt. 17, 328-330.

6 Meng, H. and Hussain, F. 1995a, In-line Recording and Off-axis Viewing (IROV) technique for holographic particle velocimetry, Appl. Opt. 34, pp. 1827-1840.

7 Meng, H. and Hussain, F. 1995b, Instantaneous flow field in a circular vortex ring captured by innovative holographic particle velocimetry, Phys. Fluids 7, pp. 9-11.

8 Pu Y and Meng H (2000): An advanced off-axis holographic particle image velocimetry (HPIV) system. Exp Fluids 29: 184-197.

9 Keane, R. D., Adrian, R. J. and Zhang, Y. 1995, Super-resolution particle image velocimetry, Meas. Sci. Technol. 6, pp. 754-768.

10 Gonzalez RC and Woods RE (1993): Digital image processing, Addison-Wesley Publishing Company, p. 502.

11 Gray, C. and Greated, C. A. 1993, Processing system for the analysis of particle displacement holograms, SPIE 2005, San Diego, pp. 636-647.

12 Huang, K., Slepicka, J. and Cha, S. S. 1993, Cross-correlation of three-dimensional images for three-dimensional three-component fluid velocity measurements, SPIE 2005, pp. 655-666.

13 Meinhart, C. D., Adrian, R. J. 1995, Measurement of the zero-pressure gradient turbulent boundary layer using particle image velocimetry, AIAA 95-0789, Wash. D. C.

14 Yang, W., Sheng, J. and Meng, H. 1998, Study of Hairpin Vortex Dynamics and Turbulence Statistics of a Surface-mounted Mixing Tab Wake Using PIV, *The 9th Int'l Symposium for Applications of Laser Techniques to Fluid Mechanics*, Lisbon, Portugal, July 13-16, 1998.

15 Yang, W. and Meng, H. 1999, Regeneration of hairpin vortices in the wake of a surface-mounted mixing tab, in preparation.

16 Gretta, W. J. and Smith, C. R. 1993, Flow structure and statistics of a passive mixing tab, J. Fluids Eng., Trans. ASME 2 pp. 255-263.

17 Elavarasan, R. and Meng 1999, H., Flow visualization study of role of coherent structures in a tab wake, submitted to Fluid Dyn. Res.